Experimental method for investigating wear of porous thermal insulation systems exposed to realistic, hot, turbulent gas flow

Reurings, C.; Koussios, S.; Bergsma, O. K.; Vergote, K.; Paeshuyse, L.; Benedictus, R.

DOI
10.1016/j.wear.2020.203536

Publication date
2021

Document Version
Final published version

Published in
Wear

Citation (APA)
Reurings, C., Koussios, S., Bergsma, O. K., Vergote, K., Paeshuyse, L., & Benedictus, R. (2021). Experimental method for investigating wear of porous thermal insulation systems exposed to realistic, hot, turbulent gas flow. *Wear*, *466-467*, Article 203536. https://doi.org/10.1016/j.wear.2020.203536

Wear 466–467 (2021) 203536

Contents lists available at ScienceDirect

Wear

journal homepage: http://www.elsevier.com/locate/wear

Experimental method for investigating wear of porous thermal insulation systems exposed to realistic, hot, turbulent gas flow

C. Reurings [a,*], S. Koussios [a], O.K. Bergsma [a,**], K. Vergote [b], L. Paeshuyse [b], R. Benedictus [a]

[a] Delft University of Technology, Aerospace Engineering, Kluyverweg 1, 2629HS, Delft, the Netherlands
[b] BOSAL ECS n.v., 20 Dellestraat, 3560, Lummen, Belgium

ARTICLE INFO

Keywords:
porous thermal insulation
Wear
Testing
Turbulent flow
High temperature
Pulsating

ABSTRACT

A realistic wear test was developed for porous thermal insulation systems exposed to high temperature turbulent gas flow, because it is essential for the development of existing and new concepts of such insulation and therefore also for the performance of processes that depend on such insulation. Wear is crucial and often dominant for the long-term performance of thermal insulation and, because of the complex nature of insulation wear under exposure of high-temperature turbulent flow, realistic testing capability is a necessary tool for improvement. A test rig was developed to subject fibrous ceramic insulation, the most encountered type of thermal insulation, to conditions representative for in-service use and to enable investigation of the occurring phenomena and behaviour. This rig can accommodate a range of different insulation configurations and is compatible with many turbulent flow sources. This test rig, its components, the experimental procedure, its accuracy and representative results are presented.

1. Introduction

1.1. Motivation

Sustainability is a major topic in the European Union and as a result there is substantial drive for improved energy efficiency. This is, amongst others, reflected in the priorities of the EU Horizon 2020 and Horizon Europe innovation programs and in the increasingly strict EU road vehicle emission legislation [1–3].

For road vehicles, the energy efficiency can be increased through lowering the vehicle mass. One possible way to do so is to replace conventional steel exhaust systems with a lower density material alternative, where, by employing thermal insulation, more materials become suitable alternatives despite the exhaust gas temperature. However, for the most cost- and mass-competitive insulation, ceramic fibres, this is a challenge in terms of performance and durability. This is to a large extent because of the combined long-term thermal and fluid-dynamic influences [4].

Improved understanding of wear of fibrous thermal insulation under combined thermal and fluid-dynamic influences can thus help in increasing vehicle energy efficiency, but it is also relevant to existing applications where insulation durability matters, such as in processing industry exhausts and ovens. More understanding of the degradation of insulation systems can also help in reducing the formation and release of the types and sizes of ceramic particles that can cause adverse health effects [5].

Realistic wear testing possibilities are crucial for developing and assessing ideas and models for the wear of fibrous insulation and also for validating designs and configurations. Testing on real systems is often not feasible because of the limited availability and associated cost and safety risk. Replacement experiments require representative fluid-dynamic and thermal conditions and realistic mounting of the insulation systems.

1.2. State of the art

There are some test rigs and methods already available; these are mentioned and analysed here. First, two from standards and then, three tests found in scientific literature. The analysis focusses on whether the test is suitable for high-temperature, high-turbulence gas flows and on the wear mechanism(s) identified, if reported.

Test standard E859 of ASTM focusses on the erosion of sprayed fire-

* Corresponding author.
** Corresponding author.
E-mail addresses: c.reurings@tudelft.nl (C. Reurings), o.k.bergsma@tudelft.nl (O.K. Bergsma).

https://doi.org/10.1016/j.wear.2020.203536
Received 18 May 2020; Received in revised form 27 October 2020; Accepted 4 November 2020
Available online 16 November 2020
0043-1648/

resistive materials lining ventilation ducts, including sprayed fibrous materials [6]. Another erosion test is part of UL 181, which is a set of standardized tests for factory-made air ducts [7]. Both standards test the wear of the material lining the duct by exposing it to an air stream and collecting fibres downstream using filters. The use of collection filters is a proven method for detecting lost fibres or fibre fragments. There is a lower limit to the captured fragment size though, so wear in the form of very small fragments can go undetected. For high temperature flow, the thermal resistance of the filter materials would have to be investigated. Also, the relatively large flows ducts and the use of collection filters is not well suited to high levels of turbulence and temperature, because of the capacity demand on the flow source.

In a set of articles Arnold, Heuer and Walter describe their measurement of wear of different configurations of fibrous insulation using a slit wind tunnel [8–10]. The thermal insulation formed both long sides of a rectangular flow channel, which was termed slit because of its small relative height of 20 mm. Their flow source was a natural gas burner and as a consequence, they achieved temperatures up to 1200 °C and a Reynolds number of $1.4{\cdot}10^4$ at that temperature and even higher at lower temperatures. The insulation wear rate was determined by counting and measuring using SEM the fibres that were sampled isostatically from the flow downstream. Accelerated embrittlement was achieved through thermal ageing before the test, i.e. by heating the samples to temperatures close to their classification temperature for a certain time interval. The fibre counting using SEM is a rather cumbersome approach and the isostatic sampling is incompatible with pulsating flows as those generated by combustion engines. Only refractory ceramic fibre insulation without cover fabric or binder was tested and it was concluded that the main wear mechanism was loss of complete fibres. The minimum detectable fibre (fragment) size was not mentioned.

Sokov and Sokov [11] have published results of a test of a different type of insulation, namely rigid fibrous hollow cylinders. These fibres are sintered together and can withstand even higher temperatures. The mass change was measured after exposure to flows with temperatures up to 1800 °C. No mention is made of mass flow rate measurements, so the Reynolds number is unknown. The presented method seems incompatible with non-rigid fibrous samples, as no provision is made to house or support them. No mention was made of the mechanics behind the wear.

Mui and Clancy [12] developed a relatively simple laboratory setup to mimic the damage of fibrous insulation systems resulting from flow exposure. A room temperature pulsating air-jet was directed at the centre of a 15 × 15 cm sample under a 45° angle to create a repeated series of traveling waves across the cover fabric. It was used in conjunction with thermal cycling to compare samples with different coatings. This approach offers a lot of freedom in terms of insulation configurations, but the thermal and flow conditions at the sample surface are not necessarily representative for those in for instance pipe flow. Consequently, this test can be used to rank the resistance of materials under the specific test conditions, but the user must determine the degree of correlation with in-service results.

The focus of their investigation was on protective coatings, so only a brief mention of the damage of the uncoated sample was made. The waves passing through the cover fabric separated and ultimately ruptured its fibres. A few seconds after the first few fibres ruptured, a hole formed in the fabric. In the provided figure, these holes in the fabric seem to occur some distance away from the through-the-thickness stitches in the insulatoin system, where the fabric was less restricted in its movement.

Besides the above mentioned articles, there is little comprehensive literature on the degradation of fibrous insulation (systems) under influence of high temperature turbulent flow. Publications on separate influences do exist, but were usually done with a different aim and were therefore not exactly representative. The authors identified the following influences that can affect the response and thus potentially also the degradation of insulation systems: the system configuration [12, 13], its interaction with the flow [14–17] and the materials and their thermal history [18–20].

The wear test presented in this article simulates in-service conditions with the benefit of flexibility in terms of sample configurations and flow sources, including compatibility with pulsating flows as those generated by combustion engines. Furthermore, it enables simple access to the sample, making mass measurement and inspection with different techniques possible.

1.3. Aim and outline of this article

A test for wear of fibrous insulation systems was designed and built that offers wall-like mechanical boundary conditions and well-defined flow conditions. During the development, the focus was on a test rig that could accommodate different insulation configurations with different mounting methods while compatible with different flow sources, including combustion engines.

The result is a test that allows wear quantification through its mass loss and visual identification of the sample state and potential damage accumulation through relatively easy intra-test inspection. The mechanical boundary conditions are such that the test rig can accommodate a range of insulation thicknesses and mounting methods. Also, as the test rig is independent of the flow source and easy to handle, the flow source can be used efficiently, because a second test rig can be coupled to the source while the first rig is, for instance, weighed, inspected or has its sample replaced.

This article firstly presents the test rig in detail, part of the test capabilities and the additional components required. Secondly, it presents the experimental procedure and thirdly, representative samples and results are shown. This includes mounting methods, mass change with time and visually observed damage mechanisms.

2. Test rig and components

2.1. Test rig

In essence, the test rig forms a closed flow channel with the sample surface forming part of the channel boundary. Along the sample, the flow channel cross-section is rectangular and it smoothly converges both up- and downstream to circular over a length of little over two pipe diameters. See Fig. 1 for an overview.

The insulation sample surface forms one of the two long sides of the rectangular flow section in the middle of the test rig, see Fig. 3 for a widthwise cross-sectional cut. The surface of other three flow channel walls is smooth steel. The rectangular section has the same hydraulic diameter as the up- and downstream circular sections, so the Reynolds number should not vary along the channel. The flow condition at the sample can thus be derived from the measurements downstream.

The test rig consists of two main components. The first and largest part of the test rig makes up the flow channel and widens on the sample side to form part of its enclosure, this is the top part in Figs. 1–4. The second part of the test rig forms the remainder of the sample enclosure, namely the bottom part in Figs. 1–4. It is in this easily replaceable part, that different mounting methods can be integrated. The bottom part is designed to be bolted to the top part. These bolt connections are through the part of the sample that extends beyond the flow channel, thus through its clamped edge, see Fig. 2.

As the sample is clamped beyond the flow channel, no special provisions are necessary for mounting it at the edge of the flow domain. Another consequence is that the sample is slightly more constrained near the sides, generally causing the wear to initiate widthwise in the middle, exactly where the flow conditions are well-defined.

The distance between the top and bottom part that defines the sample thickness is set using spacer rings around the bolts. Together with the gasket around the edge of the sample enclosure, these provide sufficient airtightness. See Fig. 1 for the spacers and gaskets. In the

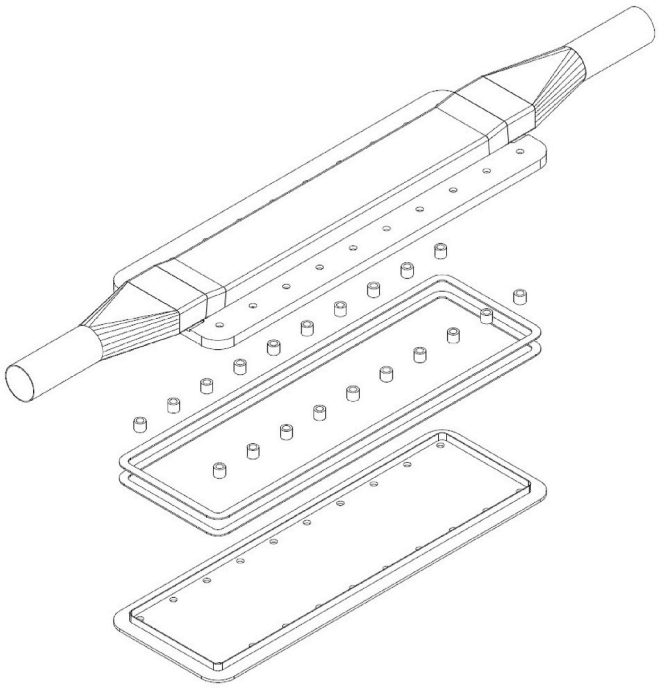

Fig. 1. Exploded view of the test rig without sample. It consists of two main components: the flow channel itself together with the top and sides of the sample enclosure, and the bottom part of the enclosure to which the sample can be mounted. In between, spacers and gaskets are mounted to control the height available to the sample and seal the circumference, respectively.

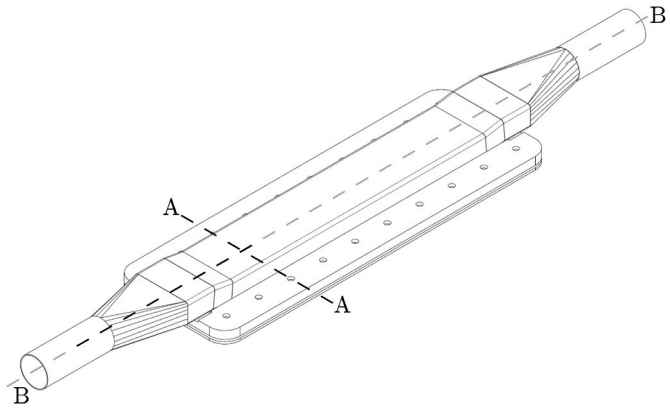

Fig. 2. An isometric view of the test rig in closed form (nuts and bolts not shown). The dashed lines A-A and B–B indicate the cross-section axes of Figs. 3 and 4.

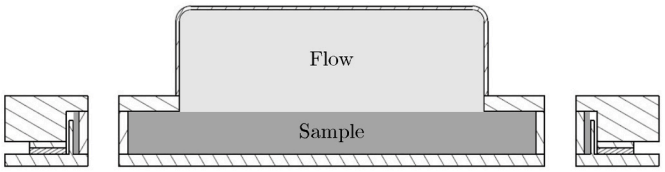

Fig. 3. Widthwise cut of the test rig, see A-A in Fig. 2. Visible are the top and bottom parts of the rig, spacing cylinders for the bolts and two stacked gaskets. The flow domain is indicated in solid light grey and the sample domain in solid dark grey.

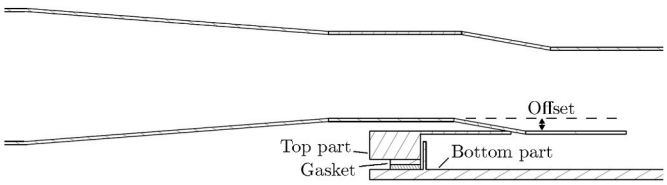

Fig. 4. Partial mid-plane lengthwise cut of the test rig, namely the bold part of line B–B in Fig. 2. From left to right, it spans from the cylindrical section to the rectangular sample section of the top part.

current configuration, the minimum thickness available to the insulation is 11 mm.

The insulation samples that can be tested using the presented rig are flat, making installation relatively simple and the setup compatible with many different configurations. In the current test rig, the length of the channel boundary that is formed by the sample is more than four times the channel width. The dimensions of the exposed area are 434 by 100 mm. The total length and width available to the sample are 593 and 170 mm, respectively. Sufficient exposed length is, first of all, necessary to make the distance over which the fully developed flow can adapt to the change in wall roughness relatively small. Second, a sufficiently long sample is necessary to be able to test insulation with spatial patterns, e.g. periodic mounting points.

The test rig was designed in such a way that its stiffness and temperature distribution limit the test rig curvature during testing with high gas temperatures. This is the reason that beyond the exposed section of the sample, the channel slopes away to a vertical offset of about 15% of the height of the rectangular channel section, see Fig. 4. Also, the spacing rings and gasket around the sample enclosure provide sufficient airtightness to prevent unwanted secondary flow through the sample. The gaskets can be stacked to accommodate different spacer heights. As the pressure difference is generally low, the stacking of gaskets provides sufficient sealing.

The test rig was made of EN 1.4301 stainless steel, providing dimensional stability at high temperatures and resistance against different gas compositions, including flue gasses. The employed gaskets were made of mica and have a maximum service temperature of 950 °C. Thermocouples were spot-welded to the test rig at specific locations to monitor the temperature evolution along the flow channel, and to record the temperature difference between the top and bottom part. In the current configuration, the test rig has been used with gas temperatures up to 800 °C. Higher gas temperatures up to 1000 °C are deemed possible, but require further investigation.

The design of the test rig is not set in stone, some aspects can be varied depending on the situation of interest. As already mentioned, the smaller bottom part can be easily replaced and adapted to different insulation mounting systems if necessary. Also, the dimensions of exposed sample area are not crucial and can be adapted to relevance, although a minimum exposure length is required to reduce the influence of entrance effects.

Furthermore, the thickness range available to the sample is not fixed. The sample thickness range of interest is primarily influenced by the insulation type and its mounting. Irrespective whether a porous sample forms a permeable or impermeable fluid boundary, the loads are largest near the flow-exposed surface [14]. The minimum possible sample thickness will therefore often be defined by the need for a realistic mechanical and thermal boundary conditions for the surface layer of the sample. When an internal combustion engine is used as a flow source, a larger sample thickness might be required for a realistic response than for steady turbulent flow because of the larger pressure variations.

The basic cylindrical connections of the test rig allow combination with different flow sources. The authors have used the test rig in combination with blowers, burners and combustion engines, but other sources are not excluded.

2.2. Experimental layout

The described test rig is the main component of the experimental setup, but it cannot function on its own. The experimental layout that was employed for the results presented in this article was as follows, from up-to downstream, Fig. 5: flow source, connection section with gas temperature measurement, test rig, connection section with gas temperature measurement and mass flow measurement. Additionally, downstream of this layout, the flow was led away from the test area to maintain a steady test environment. Furthermore, to keep the temperature of the test environment constant across time and space, active room ventilation was employed.

The analysis and study of wear requires sufficiently accurate knowledge of both sample and flow state. To assess the mass change of the sample after exposure using the afore described layout (without having to disturb the sample), the mass of the test rig including the sample was measured using a high-accuracy scale. A scale (Mettler Toledo) with a 15 kg capacity and an absolute measurement error of 0.5 g was employed. This accuracy is such that the mass has to be determined at room temperature, otherwise the buoyancy of the hot air inside will result in a bias. An uncertainty analysis according to Dunn [21] was performed to determine the uncertainty in the mass change determination of the sample, see Appendix A.

Using a heat exchanger and flow meter (ABB) the mass flow rate could be determined with about 1% accuracy. Together with the temperature, measured using K-type thermocouples, this allowed the estimation of all relevant flow properties. Fig. 6 resembles part of the setup.

3. Experimental procedure

The experimental procedure employed to obtained the results presented in this article was as follows. In order to prevent unwanted secondary flow throughout and around the sample and to determine the virgin sample mass accurately, it is important that the sample is prepared correctly to fit the enclosure. This means sizing it to the casing and punching out the holes for the bolts and spacers. Once the virgin sample mass is determined, it can be installed. Accelerated thermal ageing of samples before testing is possible. This should be done before sizing the sample to the casing as the ageing generally results in non-negligible in-plane shrinkage. The remaining steps before exposure are closing the rig at the preferred sample thickness using the spacer rings, optionally measure the leak rate to check the gasket sealing quality, and then, lastly, determine the mass of the test rig including the sample.

Once this baseline mass has been determined, the test rig can be mounted in the described experimental setup. The sample can then be exposed to the set flow for the required duration. The conditions inside the test rig can be determined from the gas flow temperature in combination with the mass flow rate and from the temperature distribution over the casing.

To assess the mass change of the sample after the exposure, the test rig has to be dismounted and allowed to cool down to room temperature. In the meantime a second test rig can be mounted to use the flow source efficiently. Once at room temperature, the mass of the test rig (including the sample) can be determined and thus the mass change with respect to the baseline mass. If required, the casing can be opened to visually inspect the sample or to apply inspection techniques. Subsequently, the casing can be mounted to the flow source again for further exposure. The whole procedure is schematically visualised in Fig. 7 and specifications are provided in Table 1.

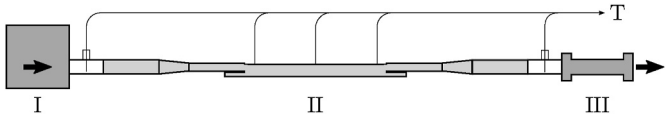

Fig. 5. Schematic representation of the test setup with, from left to right, flow source (I), test rig (II) and mass flow sensor (III). Also indicated are the locations of temperature (T) measurement.

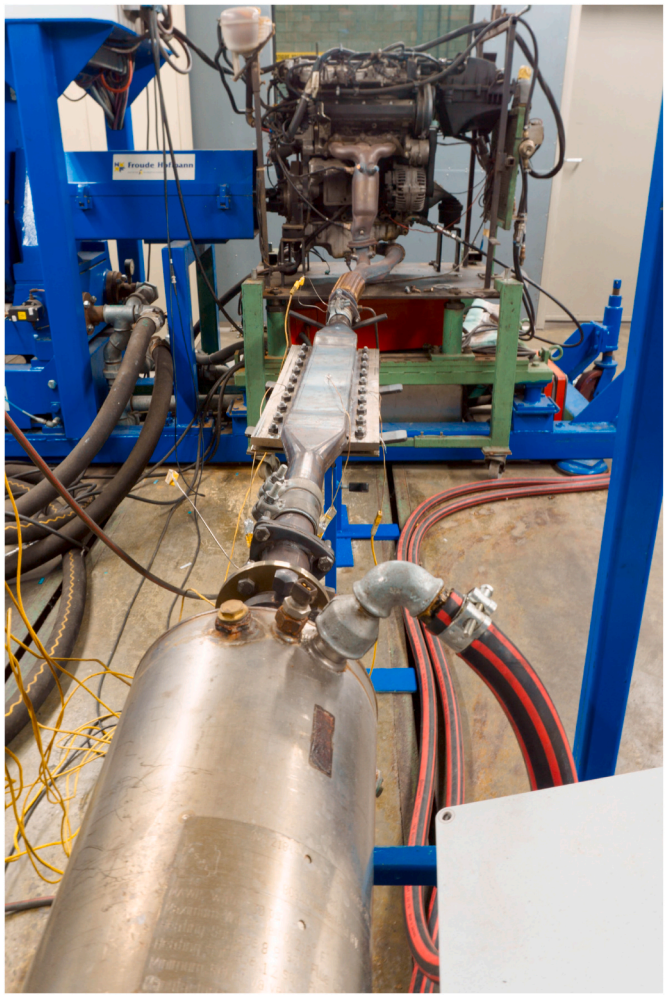

Fig. 6. The test setup as employed with a combustion engine (figure rear): downstream of the engine manifold is first the test rig with sample (figure middle), then a heat exchanger (figure front) and third a mass flow sensor (not in figure).

4. Results & discussion

A non-exhaustive set of insulation systems that can be tested using the test rig is shown here as a representative example and subsequently, for some the mass change and visual change are discussed. These examples were exposed to internal combustion engine exhaust flow (the more severe end of the test spectrum).

Many types and configurations of fibrous insulation exist and many can be tested using this test rig, some of which are presented here. Besides the insulation material itself, most configuration differences are related to the mounting, i.e. keeping the insulating fibres in place. The solutions differ between applications, but do generally include a cover fabric or liner. Figs. 8–10 depict several mounting configurations.

Table 1
Main specifications of the here presented test rig.

Current max. gas flow temperature	800 °C
Mass change uncertainty	< 0.2 g
Test rig mass	~ 15 kg
Sample size	593.2 × 170 mm
In- and outlet pipe outer diameter	54 mm

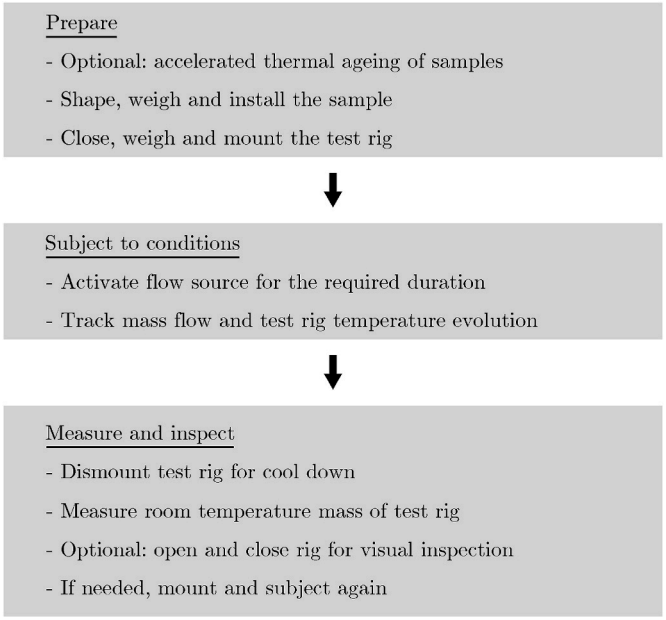

Fig. 7. Measurement procedure

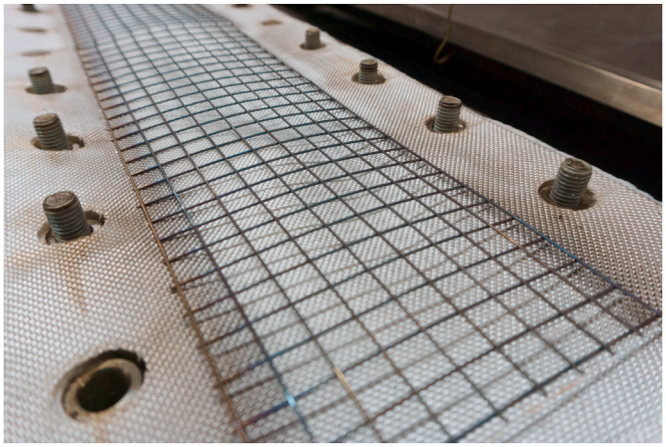

Fig. 8. Example of sample mounting: a liner with overhead thin metal mesh.

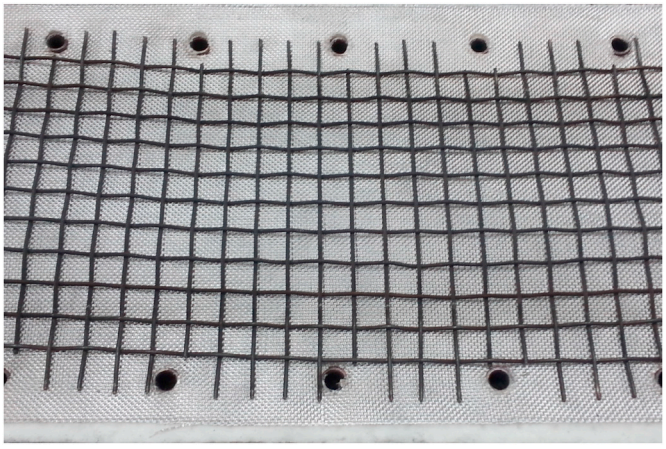

Fig. 9. Example of sample mounting: a liner with overhead thick metal mesh.

Fig. 10. Example of sample mounting: locally, the liner is mechanically connected to the bottom.

Figs. 8 and 9 show a mounting method that requires no modifications of the bottom part of the test rig, namely using a fabric liner held down by a metal mesh that spans the surface. This method offers the possibility to determine the influence of surface elements and of varying degrees of mechanical support on the wear by varying the mesh wire thickness and wire pitch. Another option is to connect the liner to another fabric underneath the insulation and adhere that to the bottom, as shown in Fig. 10.

A range of insulation system samples was exposed to gas flow until visible damage to one of the parts had occurred and their configuration was similar to that shown in Figs. 8 and 9. Given the diversity in types of degradation and the fact that some of these do not occur at the interface with the flow, makes the authors refer to the degradation in general as *wear* rather than *erosion*. Figs. 11–14 show some of the failure mechanisms that occurred. In some cases it was not the insulation that degraded the most. As shown in Fig. 11, prolonged exposure proved too much for the mounting in this case with a thin mesh.

Additionally, when testing a sample that was not thermally aged before exposure, a tear occurred in the liner after about 10 h, see Fig. 12. As this type of failure was not observed in samples with thermally aged liners, the tear was probably the result of fibre tension due shrinkage and insufficient capacity for contraction.

Fig. 13 shows a form of local insulation damage: cylindrical holes in the insulation underneath and perpendicular to the liner with a large 'shot' chunk inside. These holes suggest that these largest of shot elements do not just fall down, but keep moving around and with their large inertia, damage the surrounding fibre structure.

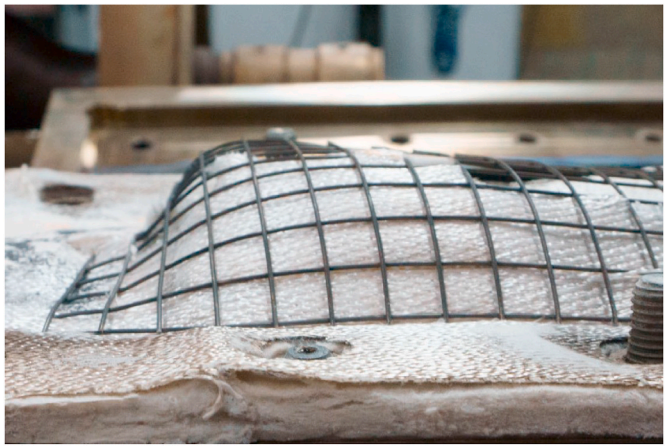

Fig. 11. Example of mounting failure rather than insulation wear.

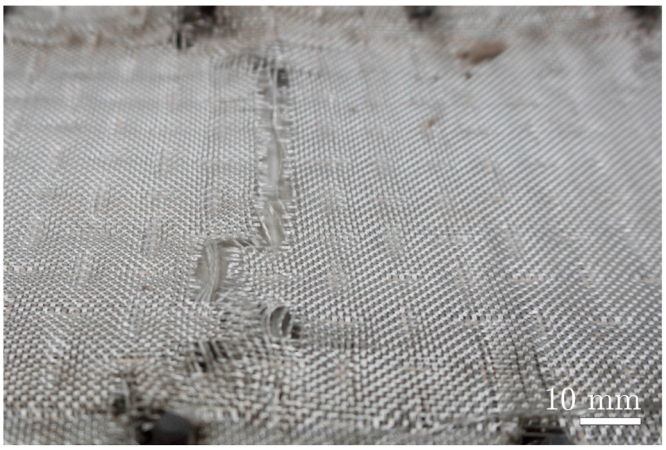

Fig. 12. Example of protective liner damage.

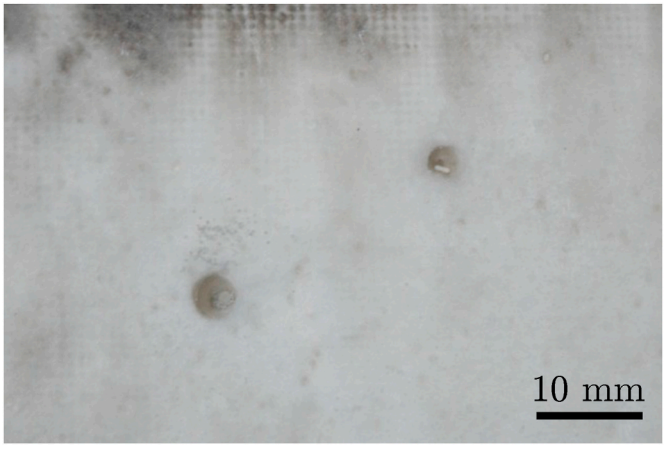

Fig. 13. Local insulation damage (wormholes), photograph taken from the flow side with the liner removed.

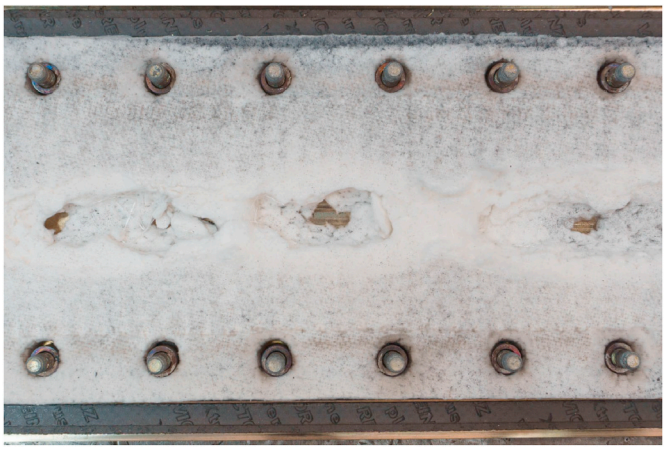

Fig. 14. Distributed insulation damage, photograph taken from the flow side with the liner removed.

In most cases however, the tested insulation systems had distributed insulation damage, which is the type that can be better correlated with the mass change. Fig. 14 shows an example. With such extensive wear, the mass change can be corrected for the presence of shot chunks in the worn region, as they remain as residue at the bottom of the sample container. This can be done by determining their mass separately after sample removal.

Representative graphs of mass change with exposure time for several fibrous insulation systems are shown in Figs. 15–17. Error bars indicating the uncertainty, see Appendix A, are included. It is assumed that the gaskets and test rig do not change in mass.

The mentioned bulk Reynolds number is defined as $\mathrm{Re}_b = u_b D/\nu_b$ and the range that was achieved with this flow source was $1{\cdot}10^4$–$4{\cdot}10^4$. It was computed using the diameter D of the pipe up- and downstream of the sample and the bulk gas flow velocity u_b derived from the mass flow using the flue gas properties, amongst which the bulk kinematic viscosity ν_b. The range of the wall-normalized frequency of the pulsations with this flow source was $\omega^+ (= \omega\nu_b/u_\tau^2) = 0.003$–$0.040$, where ω is the angular frequency of the pulsations and u_τ is the friction velocity.

The exposure duration of the un-aged sample in Fig. 15 is shorter because the sample developed a tear in the liner. To avoid interference of this local degradation with the general sample mass change, exposure was not continued. After the shown exposure durations, the liner and insulation of the samples of Figs. 16 and 17 both still lacked visible damage, proving the added value of the mass change measurement, as the absolute decrease was rather different. Additional techniques such as thermography could aid in identifying potential differences inside the insulation blankets.

Despite the difference in ageing, for all three samples of this insulation system, the observed mass change is of the order of a few percent of the sample mass. After an initial relatively large decrease the sample mass decreases more slowly with increasing exposure duration. This insulation system has blankets of amorphous ceramic fibre that contain manufacturing related residue called ‘shot’. Compared to the average fibre diameter, these chunks of shot are huge and under pressure variations, the difference in inertia will very likely stress nearby fibres. One hypothesis on the initially larger mass decrease is that it results from the larger shot elements breaking loose and falling through the network early on.

Further research, for instance comparison with shot-free fibrous insulation and insulation characterisation using microscopy before and after, is needed improve understanding of degradation of this system. This test rig makes such research feasible. For other fibrous insulation systems, however, the observed mechanisms will not be equally relevant, because of different combinations of influences, and separate investigation might be needed.

5. Conclusions

A test rig for the wear assessment of fibrous high-temperature insulation systems exposed to realistic turbulent flow was designed and built. During the development the focus was a test rig that has mechanical and fluid-dynamic conditions representative for in-service use

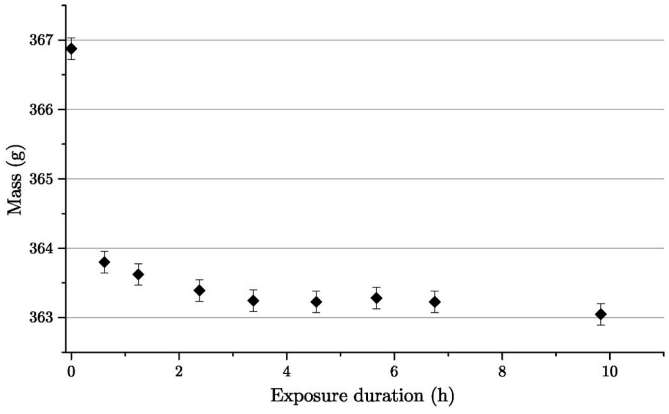

Fig. 15. Sample mass as a function of exposure time for an un-aged sample exposed to combustion engine flow (T = 700 °C, $\mathrm{Re}_b = 2.8{\cdot}10^4$)

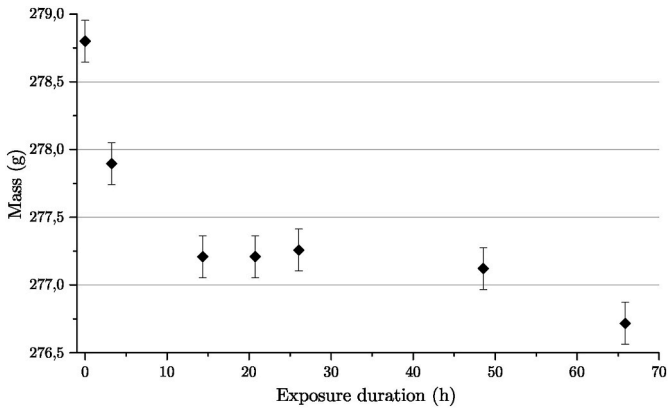

Fig. 16. Sample mass as a function of exposure time for a thermally pre-aged sample exposed to combustion engine flow (T = 690 °C, $Re_b = 2.8 \cdot 10^4$)

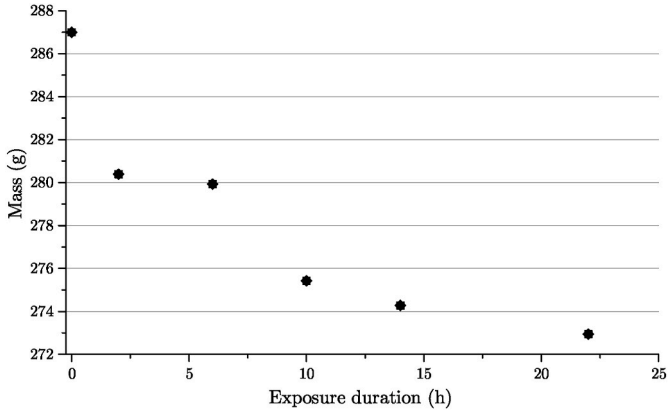

Fig. 17. Sample mass as a function of exposure time for a sample with un-aged insulation and thermally pre-aged liner exposed to combustion engine flow (T = 760 °C, $Re_b = 3.5 \cdot 10^4$)

of thermal insulation systems lining ducts or channels with high-temperature turbulent gas flows from various sources, including those that general pulsations such as combustion engines. The test rig, additional components and the experimental procedure have been introduced. The sample surface state can be visually inspected and its mass change measured without having to remove the sample from the test rig and additional techniques can be applied. Different samples have been tested under well-defined conditions, revealing different failure mechanisms and representative results have been outlined. The presented test rig can enable efficient further studies on degradation and wear of fibrous insulation systems.

Cornelis author statement

Conceptualization, investigation, formal analysis, writing – original draft.

Sotiris Koussios: conceptualization, writing – review & editing.

Otto Bergsma: conceptualization, writing – review & editing.

Karel Vergote: conceptualization, resources, writing – review & editing.

Luc Paeshuyse: conceptualization, writing – review & editing.

Rinze Benedictus: supervision, writing – review & editing.

Declaration of competing interest

The authors declare that they have no known competing financial interests or personal relationships that could have appeared to influence the work reported in this paper.

Acknowledgements

The authors would like to thank BOSAL ECS n.v. for its support and permission to publish this paper. The authors would also like to express their gratitude for the technical support offered by Bernard Lehaen, Dave Mariën and Dirk Vanderheyden.

Appendix A. . Uncertainty analysis

The uncertainty in the mass change as obtained in the here presented measurement procedure was estimated using the method outlined by Dunn [21]. Differentiation between the contributions of different sources of error allows an estimate of the uncertainty in the final result. The method is based on probabilistic considerations, which means that the random and systematic errors are all described in terms of Gaussian distributions. In this case three sources of error were included, two random ones and one systematic.

Because the mass can be measured directly and the mass difference is simply the subtraction of two consecutively measured masses, the uncertainty of the scale has a large influence. It has both a random variation (influence on the average) and a bias (systematic error). The former, the random uncertainty of the average value, was obtained from the standard deviation of the set of mass measurements $S_{P_{sc}}$ as used to compute the average:

$$S_{\overline{P}_{sc}} = \frac{S_{P_{sc}}}{\sqrt{N}} \tag{A.1}$$

where N is the number of measurements in the set, resulting in $S_{\overline{P}_{sc}} = 0.01$g. The latter, the standard deviation of the bias error of the mass measurement using the mentioned scale, was estimated by assuming that the manufacturer-specified accuracy (0.5g) represents the 95% confidence level bias limit. This means that the standard deviation is roughly half the limit: $S_{B_{sc}} = 0.25$g.

The last source of error, which is also random, is the variation in conditions for the different mass measurement series. Its contribution was estimated based on repeated test rig mass measurements at different occasions. The resulting standard deviation $S_{\overline{P}_{co}}$, while taking into account the Student's t distribution, was 0.04 g.

The expression for the combined standard uncertainty for the mass change, u_r, requires the determination of the absolute sensitivity coefficients θ_i for the different average masses. In this case, these are the derivatives of the expression for the mass change $r = x_1 - x_2$ with respect to the two different measurands x_1 and x_2, where the measurands represent the sample mass before and after the (continued) exposure, respectively. Leading to $\theta_1 = \partial r/\partial x_1 = 1$ and $\theta_2 = \partial r/\partial x_2 = -1$.

A look at the resulting expression for the combined standard uncertainty reveals that the bias error will cancel out since it is common to both

measurements. This leaves only the two random contributions. Since these are not common to both mass measurements, their covariances are zero. The remaining expression for the total uncertainty in the mass change at a 95% confidence level is then:

$$U_{mass,95} = t_{\nu_r,95} u_r \tag{A.2}$$

with.

$$u_r^2 = \theta_1^2 S_{\bar{P}_{sc}}^2 + \theta_2^2 S_{\bar{P}_{sc}}^2 + \theta_1^2 S_{\bar{P}_{co}}^2 + \theta_2^2 S_{\bar{P}_{co}}^2 \tag{A.3}$$

and $t_{\nu_r,95}$ is the Student's t distribution. Substitution of the values and the number of degrees of freedom results in a total uncertainty in the mass change at a 95% confidence level of $U_{mass,95} = 0.16$ g.

References

[1] European Commission, Horizon 2020: key enabling technologies. https://ec.europa.eu/programmes/horizon2020/en/area/key-enabling-technologies.

[2] European Commission, Commission Launches Work on Major Research and Innovation Missions for Cancer, Climate, Oceans and Soil, July 2019. https://ec.europa.eu/info/news/commission-launches-work-major-research-and-innovation-missions-cancer-climate-oceans-and-soil-2019-jul-04_en.

[3] European Parliament, The Council, Regulation (EU) 2019/631 of the European Parliament and of the Council of 17 April 2019 Setting CO^2 Emission Performance Standards for New Passenger Cars and for New Light Commercial Vehicles, and Repealing Regulations (EC) No 443/2009 and (EU) No 510/2011, Official Journal of the European Union, 2019.

[4] P.M. Sawko, H.E. Goldstein, Performance of Uncoated AFRSI Blankets during Multiple Space Shuttle Flights, NASA Technical Memorandum 103892, National Aeronautics and Space Administration, 1992.

[5] T.P. Brown, P.T.C. Harrison, Crystalline silica in heated man-made vitreous fibres: a review, Regul. Toxicol. Pharmacol. 68 (2014) 152–159, https://doi.org/10.1016/j.yrtph.2013.11.014.

[6] ASTM International, ASTM Standard E859, Standard Test Method for Air Erosion of Sprayed Fire-Resistive Materials (SFRMs) Applied to Structural Members, 2011, https://doi.org/10.1520/E0859-93R11.

[7] Underwriters Laboratories, Ul 181 - standard for factory-made air ducts and air connectors. http://www.ul.com, 2013.

[8] F. Arnold, V. Heuer, G. Walter, Zur wirkung von strömungsbeanspruchungen auf die beständigkeit von fasernbauteilen in industrieöfen, Gaswärme Int. 45 (6) (1996) 285–289.

[9] V. Heuer, G. Walter, Wear of fibrous ceramic components caused by high velocity gas streams: erosion mechanisms, Ceram. Forum Int./Ber. DKG 75 (11–12) (1998), 29–35, cfi-Ceram Forum Int.

[10] V. Heuer, G. Walter, F. Arnold, Zu den einsatzgrenzen keramischer faserbauteile in thermischen anlagen bei hohen gasgeschwindigkeiten, Gaswärme Int. 47 (6) (1998) 325–331.

[11] V.N. Sokov, V.V. Sokov, Fibrous nanocorundum products for use in a high-temperature gas flow, Refract. Ind. Ceram. 53 (6) (2013) 379–383, https://doi.org/10.1007/s11148-013-9530-x.

[12] D. Mui, H.M. Clancy, Development of a protective ceramic coating for shuttle orbiter advanced flexible reusable surface insulation (afrsi), Ceram. Eng. Sci. Proc. 6 (1985) 793–805, https://doi.org/10.1002/9780470320280.ch31.

[13] K. Keller, J. Antonenko, K.H. Weber, High-temperature insulations, ESA Bull. 80 (1994) 50–56.

[14] W.-P. Breugem, B.J. Boersma, R.E. Uittenbogaard, The influence of wall permeability on turbulent channel flow, J. Fluid Mech. 562 (2006) 35–72, https://doi.org/10.1017/S0022112006000887, j Fluid Mech.

[15] C. Manes, D. Pokrajac, I. McEwan, V. Nikora, Turbulence structure of open channel flows over permeable and impermeable beds: a comparative study, Phys. Fluids 21 (12) (2009) 1–12, https://doi.org/10.1063/1.3276292.

[16] K. Suga, Y. Matsumura, Y. Ashitaka, S. Tominaga, M. Kaneda, Effects of wall permeability on turbulence, International Journal of Heat and Fluid Flow vol. 31 (6) (2010) 974–984, https://doi.org/10.1016/j.ijheatfluidflow.2010.02.023, int J Heat Fluid Fl.

[17] C. Reurings, S. Koussios, O.K. Bergsma, W.-P. Breugem, K. Vergote, L. Paeshuyse, R. Benedictus, The influence of a porous, compliant layer with overlying discrete roughness elements as exhaust pipe wall on friction and heat transfer, Heat Mass Tran. 56 (2020) 2367–2387, https://doi.org/10.1007/s00231-020-02855-4.

[18] I. Zaplatynsky, Shrinkage of amorphous silica fibers, in: W. Smothers (Ed.), Proceedings of the 7th Annual Conference on Composites and Advanced Ceramic Materials, vol. 44, John Wiley & Sons, 1983, pp. 492–501, https://doi.org/10.1002/9780470320129.ch3, of Ceramic Engineering and Science Proceedings Series.

[19] V. Heuer, G. Walter, I. Hutchings, High Temperature Erosion of Fibrous Ceramic Components by Solid Particle Impact, Wear vols. 233–235 (1999) 257–262, https://doi.org/10.1016/S0043-1648(99)00223-9.

[20] T. Tonnesen, P. Dietrichs, R. Telle, Linear shrinkage, resilience and microstructural changes in high temperature insulating wools in maximum use temperature range, Advances in Applied Ceramics 104 (5) (2005) 249–255, https://doi.org/10.1179/174367605X46812.

[21] P.F. Dunn, Measurement and Data Analysis for Engineering and Science, second ed., CRC Press, Boca Raton, FL, USA, 2010.